Automated operational modal analysis and ambient noise deconvolution interferometry for the full structural identification of historic towers: A case study of the Sciri Tower in Perugia, Italy

Enrique García-Macías[a,*], Filippo Ubertini[a]

[a]*Department of Civil and Environmental Engineering, University of Perugia, Via G Duranti 93, Perugia 06125, Italy*

Abstract

Structural Health Monitoring (SHM) based upon Operational Modal Analysis (OMA) constitutes an increasingly mature and widespread technology in the conservation of historic structures. Such techniques, while proved effective for assessing the global integrity of structures, may fail at detecting local damage with little influence on the modal features of the system. In this context, the analysis of propagating waves throughout the structure features a synergistic approach to OMA with superior capabilities for data-driven damage identification. Although some promising results have been reported in the literature on the application of Seismic Interferometry to reinforced-concrete structures, works concerning the continuous monitoring of ambient vibrations in historic structures are virtually non-existent. In this light, this paper proposes the coupled application of automated OMA and Ambient Noise Deconvolution Interferometry for the full structural system identification of historic structures, and evaluates the advantages of this technology through a validation case study of the Sciri Tower in Perugia, Italy. A continuous vibration-based monitoring system deployed in the tower during three weeks allows us to assess the effectiveness of the proposed approach. The reported results demonstrate the robustness of the monitoring system for identifying environmental effects on the spatial distribution of wave velocities, and shed light into the dispersion relation of the tower.

Keywords: Ambient vibration testing, Automated Operational Modal Analysis, Seismic Interferometry, Structural Health Monitoring, Wave propagation

---

1. Introduction

Structural Health Monitoring based on output-only or OMA has become a mature and ubiquitous technology in the preventive maintenance of structures. These techniques exploit ambient acceleration records to extract the modal properties of the structure as damage sensitive features [1–3]. Given that these systems work under operational conditions, the degree of invasiveness and impact on the monitored structure are minimal [4–7], so their implementation in Cultural Heritage (CH) structures has become particularly popular (see e.g. [8–12]). Due to the sensitivity of the modal properties to environmental factors, such as temperature or humidity [13, 14], damage is often masked by daily modal fluctuations, so long-term monitoring schemes are essential to fully exploit the potential of modal-based damage detection techniques. In this wise, automated OMA techniques allow the continuous and remote assessment of the structural health, maximizing their capability for early damage detection through novelty analysis and improving their usefulness for decision-making in maintenance and rehabilitation activities. Nevertheless, while proved highly effective for interrogating the global integrity of structures, these techniques may be inefficient in detecting local damage with little influence on the modal features of the system. Moreover, the localization of local structural pathologies usually requires the inverse calibration of a numerical model which, in the case of historical buildings, may be computationally demanding and incompatible with continuous monitoring systems. In this context, seismic interferometric techniques represent a synergistic approach to OMA with superior capabilities for data-driven damage identification. Nonetheless, while a few promising results have been reported in the literature on its application for earthquake-induced damage detection of reinforced-concrete structures, works coping with the use of Seismic Interferometry for the continuous monitoring of structures under ambient conditions are very scarce, and practically non-existent in the realm of historic buildings.

Seismic interferometry conceives the response of a dynamic system as a superposition of propagating waves, and exploits the wave velocities between pairs of sensors as damage sensitive features [15–17]. The fundamentals

*Corresponding author.
Email address: `enrique.garciamacias@unipg.it` (Enrique García-Macías)

of this approach lie in the fact that scattering and attenuation of propagating pulses depend upon the constitutive properties of the medium and, therefore, the identification of wave velocities provides an indirect evaluation of the intrinsic stiffness of the system [18]. To do so, travelling waveforms can be described by means of impulse response functions (IRFs) computed at different monitored locations throughout the structure. Specifically, IRFs obtained by deconvolution interferometry have proven well-suited for the monitoring of mono-dimensional structures such as buildings or towers [19, 20]. Recent research works report promising advantages of seismic interferometric techniques compared to OMA-based approaches. In the first place, damage identification based upon Seismic Interferometry is local in essence, since damage-induced stiffness deterioration leads to localized increases in the pulse travel times across the damaged part of the structure [21–23]. Most interestingly, damage identification (detection, localization and, to some extent, quantification) can be performed in a fully data-driven way simply by peak-picking analysis of IRFs [24]. A second distinctive feature of these techniques regards the possibility of investigating soil-structure interaction (SSI) properties through the analysis of the dispersion of seismic waves [25–27]. Dispersive media are characterized by the variation of phase velocities with frequency. It has been reported that the contribution of bending deformation to the dynamic response of the structure (as it is usually the case of high-rise buildings), as well as SSI effects, increase the dispersion of seismic waves [27, 28]. Nevertheless, as demonstrated by the work of Rahmani et al. [27], wave velocities estimated from broader band IRFs (including at least two modes of vibration) show almost no sensitivity to the SSI, and primarily provide information about the specific condition of the building irrespective of the boundary conditions at the foundation.

The broad majority of research on the application of Seismic Interferometry to structural system identification has focused on reinforced-concrete (RC) buildings under seismic actions. The assessment of wave travel times using IRFs was first proposed by Snieder and Şafak [17], who studied the wave propagation properties of the 9-storey RC Millikan Library in Pasadena (Los Angeles, US) during the Yorba Linda M_w 4.3 earthquake in 2002. Their results showed that the IRFs reflect well the propagation mechanisms of seismic waves across the building, reporting acausal upgoing and downgoing (reflected) pulses when the deconvolution is referenced to the roof level, and only causal pulses propagating upward when referenced to the base. A similar methodology was applied by Todorovska and Trifunac [29] for the analysis of the Van Nuys 7-story hotel under different earthquakes. Specifically, their results demonstrated considerable wave delays (decrease in stiffness) during the 1994 Northridge and 1971 San Fernando earthquakes, which agree well with the observed damage by separate inspections. Those authors also investigated the effects of the Imperial Valley Earthquake of 1979 on the wave propagation properties of a 6-storey RC building in El Centro (California, US) [22], and their results reported good agreements between the wave delays obtained by peak-picking of IRFs and the actual earthquake-induced damage. Rahmani and Todorovska [30] proposed an SHM system based on the fitting of wave velocity profiles by the inverse calibration of an equivalent layered shear beam model. Their results showed that, given that the calibration essentially involves phase differences between motions at different floors of the building, the identified velocity profile is minimally affected by SSI and, therefore, provides a superior damage-sensitive feature compared to OMA-based approaches. Nonetheless, although most of the mechanisms underlying the propagation of seismic waves in multi-storey buildings could be explained, the shear beam model failed to reproduce the observed dispersion effects. In order to address this issue, Ebrahimian and Todorovska [28, 31] developed a layered Timoshenko beam (TB) model accounting for both shear and bending deformation effects for wave propagation analysis. Their results demonstrated the contribution of bending deformation to the dispersion of travelling waves. The resulting dispersion relation (phase velocity versus frequency) was proved monotonically increasing with frequency, with largest velocity variations at low frequencies and stable values at high frequencies. Interestingly, those authors also reported the existence of two propagating modes with different phase velocities in high-rise buildings. Below a certain critical frequency depending on the material properties and geometry of the building, one single mode defines the wave propagation, while both modes determine the waveforms above this cut-off frequency generating complex interference patterns. Recently, the authors [32] extended the TB formulation to investigate the application of acceleration- and strain-based wave propagation analysis for damage identification in masonry towers under seismic actions. Using pseudo-experimental records generated by a non-linear 3D numerical model, the reported results demonstrated that the inverse calibration of the TB model allows relating identified damage-induced wave delays to local stiffness losses in the structure.

The number of works on the use of Deconvolution Interferometry for the system identification of structures under ambient vibrations is considerably lower. Among them, a noteworthy contribution is the work by Prieto *et al*. [33] who applied Ambient Noise Deconvolution Interferometry (ANDI) for the system identification of the 17-storey steel moment-frame UCLA Factor building located at the University of California. In that work, IRFs were generated from ambient noise by means of a deconvolution approach with temporal averaging. A similar technique was also used by Nakata and Snieder [34] for the monitoring of an 8-storey building in Japan. Interestingly, their results showed that ambient noise IRFs are characterized by causal and acausal pulses when deconvolution is referenced to both the base and the roof levels. Such a behaviour, unlike the case of seismic excitation, is due to the presence of several excitation sources throughout the building (e.g. micro-tremors, human actions, wind loadings). Bindi *et al*. [35] conducted ambient vibration tests (AVTs) on an 8-storey RC hospital in Thessaloniki (Greece), and explored the simultaneous application of ANDI and Frequency Domain Decomposition (FDD). Their results suggested the possibility of developing SHM systems based upon the synergistic application of OMA and ANDI for full system identification. In this regard, Lacanna *et al*. [36] conducted a pioneering application of continuous OMA and ANDI for structural assessment of the Giotto's bell-tower in Florence, Italy. Despite reporting some limitations for the identification of environmental effects on the wave velocities due to insufficient sampling frequency and short monitoring time, their results evidenced the superior capabilities of SHM systems based on automated OMA/ANDI for damage detection, localization, and quantification. Recently, the authors reported in reference [37] the synergistic application of OMA and ANDI for the full dynamic identification of three different architectural heritage structures using AVTs, including the Sciri Tower in Perugia, the Consoli Palace in Gubbio, and the bell-tower of the Basilica of San Pietro in Perugia. While promising, the reported results highlighted the existence of substantial environmental effects on the identified wave velocities, and thereby discrete AVTs are often ineffective to extract damage sensitive features. In these cases, the continuous monitoring of structures and the characterization of environmental effects become imperative for performing pattern recognition and effective damage identification, as addressed in this work.

In light of the previous state-of-the-art review, this paper proposes the coupled application of automated OMA and ANDI for the full structural system identification of historic structures, and evaluates the advantages of this technology through a validation case study of the Sciri Tower in Perugia, Italy. This case study represents a standard example of a masonry tower inserted into a building aggregate, and a continuous vibration-based monitoring system installed in the tower during three weeks allows us to assess the effectiveness of the proposed approach. The reported results evaluate the robustness of the monitoring system for identifying environmental effects on the spatial distribution of wave velocities, and shed some light into the dispersion relation of the tower.

The remaining of this paper is organised as follows. Section 2 describes the Sciri Tower and the monitoring system installed in the structure. Section 3 presents the system identification results obtained by automated OMA. Section 4 reports the results obtained by ANDI, and investigates the environmental effects of the wave velocity profiles in two orthogonal directions of the tower and, finally, Section 5 concludes this work.

2. Description of the Sciri Tower and testing set-up

The Sciri Tower (*Torre degli Sciri*) is a 41 m high civic tower located in the historical centre of Perugia in Italy. Its construction dates back to the late 13$^{\text{th}}$ century and, nowadays, the Sciri Tower is the only one preserved intact among the numerous towers erected during the medieval period of the city. The tower was owned by the noble family of Oddi until 1488, when it was transferred to the Sciri family (who gave it its current name) after violent disputes between noble clans that forced the Oddi family into exile. In 1680, the tower and the adjoining building were gifted to the Franciscan Third Order until 2011, when the ensemble became property of the Municipality of Perugia. Important conservative restoration works were conducted in the building ensemble by the municipality in 2015, although neither the building aggregate nor the tower experienced significant structural modifications.

The Sciri Tower is inserted into a building ensemble with approximate plan dimensions of 22×25 m. The tower is made of homogeneous squared white limestone blocks and has a hollow rectangular cross-section of 7.15×7.35 m, with three façades connected to the adjacent masonry buildings up to a height of 17 m, and a fourth one remaining unconstrained all along its height. The tower can be ideally split into two structural portions beneath and above the height level of 8.4 m. The lower part has wall thicknesses between 1.68 m and 2.1 m, and culminates with a stone masonry vaulted slab standing over an old chapel. On the other hand, the upper part has slender continuous walls (with thickness varying in height from 1.6 m to 1.4 m), and houses a metal staircase resting on four 1.5 m wide masonry vaulted slabs at different heights. Finally, a brick masonry ceiling vault completes the tower, and a 0.5 m thick parapet along the edges of a panoramic terrace rises up to a total height of 41 m.

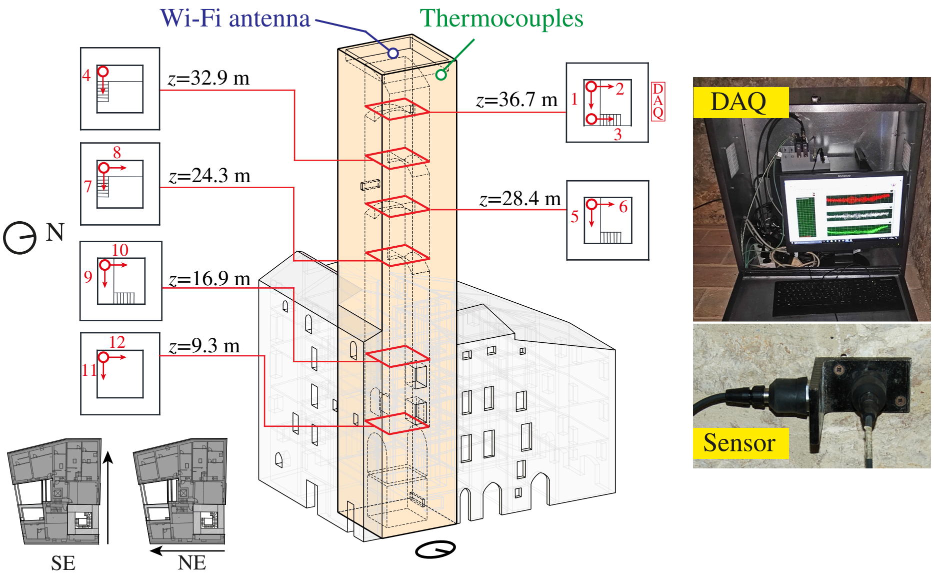

Figure 1: Layout of the dynamic monitoring system installed in the Sciri Tower with sensors positions (labelled from 1 to 12).

With the aim of identifying the modal features and wave propagation properties of the Sciri Tower, a continuous ambient vibration testing was performed for three weeks, from February 13th until March 10th 2019. To this end, a total of 12 high sensitivity (10 V/g) uniaxial PCB 393B12 accelerometers were installed at four different heights of the tower, namely z = 40.5 m, z = 33.5 m, z = 24.0 m and z = 8.4 m, as shown in Figure 1. Ambient vibrations were recorded at three different sampling frequencies to evaluate the robustness of the wave identification, including 200 Hz, 1000 Hz, and 5000 Hz. In addition, two K-type thermocouples were also installed at the level z = 40.5 m (indoor and outdoor) and temperature was recorded at a sampling frequency of 0.4 Hz. Field data were acquired using a multi-channel data acquisition system (DAQ) model NI CompactDAQ-9184 located at the level z = 36.7 m, equipped with NI 9234 data acquisition modules for accelerometers (24-bit resolution, 102 dB dynamic range and anti-aliasing filters) and NI 9219 modules for thermocouples (24-bit resolution, ±60 V range, 100 S/s). A LabView toolkit was implemented for data acquisition and preliminary real-time processing, including amplitude and spectral plots for quality-control inspections. Data were recorded in separate files containing 30-min long acceleration and temperature time series, and transferred in real-time through Wi-Fi connection to the Laboratory of Structural Dynamics of the University of Perugia, 2.5 km far from the tower. Here, data were stored and processed with the purpose of extracting the dynamic characteristics of the tower, including its modal properties and wave propagation velocities. Figure 2 shows a flowchart of the automated OMA and ANDI system implemented in the Sciri Tower, the details of which are described hereafter.

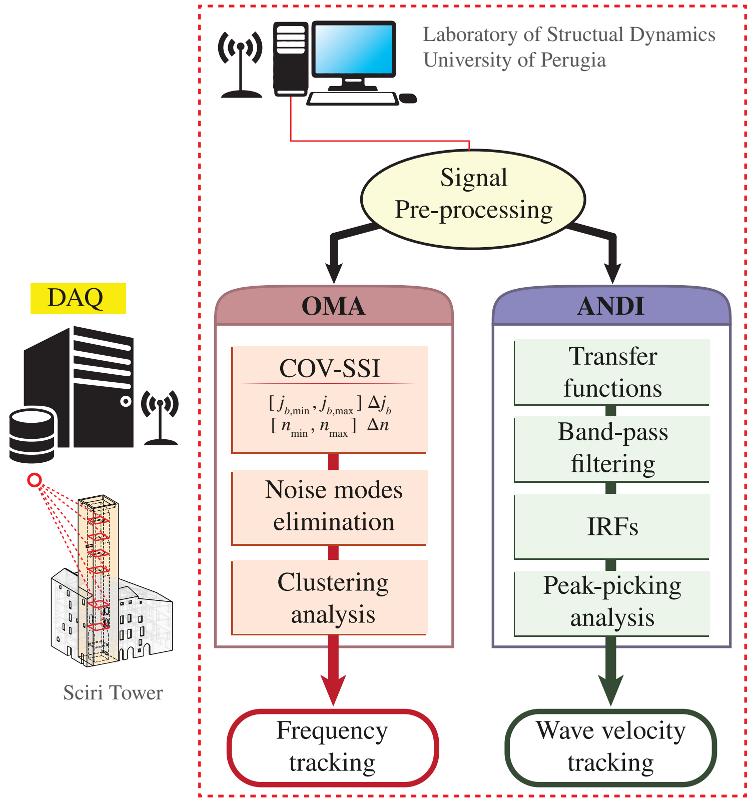

Figure 2: Flowchart of the automated OMA and ANDI system implemented in the Sciri Tower.

3. Automated Operational Modal Analysis

3.1. Automated OMA algorithm

The Covariance-driven Stochastic Subspace Identification (COV-SSI) method [38] has been used to perform the online OMA of the Sciri Tower. In particular, an in-house fully automated OMA code has been implemented in MATLAB environment following an automation approach equivalent to the one proposed by Ubertini *et al.* [39]. This consists of three consecutive steps as sketched in Fig. 2, including iterative modal identification (i), noise modes elimination (ii), and clustering analysis (iii). The first step consists of performing the modal identification considering an interval $[j_{b,min}, j_{b,max}]$ with steps of size Δj_b of the number of blocks of the Toeplitz matrix in the COV-SSI method, as well as an interval of model orders $[n_{min}, n_{max}]$ with steps of size Δn. This procedure results in a set of M poles, whose modal information can be organized in matrix form as:

$$\begin{aligned}\mathbf{f} &= [f_1\, f_2\, \ldots\, f_M]^{\mathrm{T}}\,,\\ \boldsymbol{\zeta} &= [\zeta_1\, \zeta_2\, \ldots\, \zeta_M]^{\mathrm{T}}\,,\\ \boldsymbol{\Theta} &= [\boldsymbol{\Theta}_1\, \boldsymbol{\Theta}_2\, \ldots\, \boldsymbol{\Theta}_M]\,,\end{aligned} \tag{1}$$

where f_m, ζ_m, and $\boldsymbol{\Theta}_m$ denote the frequency, damping, and mode shape vector of an arbitrary m-th mode, $m = 1, 2, \ldots, M$. Afterwards, a noise modes elimination algorithm is implemented in order to automate the analysis of the multiple resulting stabilization diagrams. This algorithm discerns between noise modes and physical ones by assessing the frequency of appearance of the system poles over all the identification analyses. To do so, a vector $\mathbf{c} = [c_1\, c_2\, \ldots\, c_M]^{\mathrm{T}}$ is constructed, whose components c_m, $m = 1, 2, \ldots, M$, are given by:

$$c_m = \begin{cases} -1 + \sum_{l=1}^{M} \delta_{lm}, & \text{if} \quad \zeta_m \in [0\, \zeta_{max}] \\ 0, & \text{if} \quad \zeta_m \notin [0\, \zeta_{max}] \end{cases} \tag{2}$$

with

$$
\begin{aligned}
&\delta_{lm} = \begin{cases} 1, & \text{if} \quad \Delta f_{lm} \le \epsilon_f,\ \Delta\zeta_{lm} \le \epsilon_\zeta,\ 1 - MAC_{lm} \le \epsilon_{MAC} \\ 0, & \text{otherwise} \end{cases} \\
&\Delta f_{lm} = \frac{|f_l - f_m|}{f_m},\ \Delta\zeta_{lm} = \frac{|\zeta_l - \zeta_m|}{\zeta_m},\ MAC_{lm} = MAC(\boldsymbol{\Theta}_l, \boldsymbol{\Theta}_m),
\end{aligned} \tag{3}
$$

where ζ_{max} is the maximum admissible value for the damping ratio of the physical modes, $MAC(\boldsymbol{\Theta}_l, \boldsymbol{\Theta}_m)$ is the Modal Assurance Criterion (MAC) value between modes Θ_l and Θ_m, and ϵ_f, ϵ_ζ, and ϵ_{MAC} are user-defined tolerances. A generic component, c_m, indicates the number of modes with frequencies, damping ratios, and mode shapes similar to those of the m-th mode among all the M identified ones. Therefore, the m-th mode is said to be stable when its frequency of appearance given by c_m is larger than a certain fraction s of the total number of modal identification analyses N, i.e. $c_m \ge sN$. Then, the number of stable poles can be readily obtained computing a vector $\mathbf{S}$:

$$
\begin{aligned}
&\mathbf{S} = [S_1\, S_2\, \dots\, S_M]^{\mathrm{T}}, \\
&S_m = \begin{cases} 1, & \text{if} \quad c_m \ge sN = s\left(\frac{j_{b,max} - j_{b,min}}{\Delta j_b} + 1\right)\left(\frac{n_{max} - n_{min}}{\Delta n} + 1\right) \\ 0, & \text{otherwise} \end{cases}
\end{aligned} \tag{4}
$$

whose components S_m assign 0 and 1 to unstable and stable modes, respectively. Consequently, the total number of stable modes, P, simply reads $P = \sum_{l=1}^{M} S_l$. The vectors of stable frequencies $\mathbf{f}^s$ and damping ratios $\boldsymbol{\zeta}^s$, and the matrix of stable mode shapes $\boldsymbol{\Theta}^s$ can be extracted as:

$$
\begin{aligned}
\mathbf{f}^s &= \mathbf{HE}\,\mathbf{f} = [f_1\, f_2\, \dots\, f_P]^{\mathrm{T}}, \\
\boldsymbol{\zeta}^s &= \mathbf{HE}\,\boldsymbol{\zeta} = [\zeta_1\, \zeta_2\, \dots\, \zeta_P]^{\mathrm{T}}, \\
\boldsymbol{\Theta}^s &= \left(\mathbf{HE}\,\boldsymbol{\Theta}^{\mathrm{T}}\right)^{\mathrm{T}} = [\boldsymbol{\Theta}_1\, \boldsymbol{\Theta}_2\, \dots\, \boldsymbol{\Theta}_P],
\end{aligned} \tag{5}
$$

where $\mathbf{HE}$ is a $P \times M$ matrix whose non-zero components are $HE_{p,\pi_p} = 1$, $p = 1, 2, \dots, P$, with $\pi_1, \pi_2, \dots, \pi_p$ being the positions of the non-zero terms of vector $\mathbf{S}$.

Finally, an agglomerate hierarchical clustering algorithm is implemented to group the previously extracted P stable modes into a set of homogeneous data clusters pertaining to the same structural mode. Interested readers may refer to reference [38] for further details on the implemented clustering analysis procedure.

3.2. Initial ambient vibration test

The identification results of the first 30-min long vibration records, taken on February 13th 2019 at 2:00 pm and down-sampled to 40 Hz, are presented in Fig. 3 and Table 2. The raw data were initially pre-processed by subtracting the temporal mean and applying time-domain Hanning filtering to eliminate undesired noise sources such as spikes related to electrical interferences. For validation purposes, Table 2 collects the identified natural frequencies and damping ratios obtained by four different OMA methods, namely the COV-SSI, Eigensystem Realization Algorithm (ERA), poly-reference Least Squares Complex Frequency-domain (p-LSCF), and Enhanced Frequency Domain Decomposition (EFDD) methods [38]. The input parameters used in the considered identification methods are collected in Table 1. The ERA method has been implemented following an automated procedure identical to the one previously reported in Section 3.1, with j_b denoting in this case the number of block rows and columns of the Hankel matrix of the cross-correlation functions. Readers are referred to the Supplementary Material for further details on the OMA of the Sciri Tower.

Seven vibration modes have been identified in the frequency range between 0 and 12 Hz, including two flexural modes in the NE direction (Fx1 and Fx2), two flexural modes in the SE direction (Fy1 and Fy2), one torsional mode (Tz1), and two higher order flexural modes, (Fx3 and Fy3). It is noted in Table 2 that all the identification methods yield very close estimates of the resonant frequencies with relative differences below 2%. Nevertheless, considerable discrepancies can be observed in terms of damping ratios between the time-domain (COV-SSI and ERA) and frequency-domain (p-LSCF and EFDD) identification methods. The frequency-domain methods report considerably smaller damping ratios, with values even below 0.2% which are assumed as unidentified damping values. In particular, the p-LSCF method failed to identify the damping ratios of modes Fx3 and Fy3. It is well-known in the literature that, while very clear stabilization diagrams are obtained with the p-LSCF method, this technique tends to underestimate the damping parameters of low-excited modes with high noise levels [40], as it is the case of most historic masonry structures. Advanced system identification methods such as the combination of the maximum likelihood estimator and the p-LSCF method (ML-pLSCF, see [41]) have been reported to alleviate such limitations. Finally, it is noted that the EFDD method yields unrealistically low damping ratios for modes Fy2, Tz1, Fx3 and Fy3, which is due to a poor representation of their single mode bell functions and the corresponding correlation functions. This issue is also conceivably due to an insufficient excitation levels for these modes.

In light of the previous discussion, the COV-SSI method is used in this work in all the subsequent analyses. The corresponding mode shapes obtained by COV-SSI are depicted in Fig. 3. In this figure, complexity plots of the identified mode shapes are also shown, where each arrow represents a component of the mode shape vectors. The more collinear the components are the more the system is classically (proportionally) damped in that mode. Conversely, scatters in the complexity plot may indicate that the system is non-classically damped in that mode, or may evidence the presence of limiting factors in the identification, such as low signal-to-noise ratios, estimation or modelling errors. It is noted in Fig. 3 that modes Fx1, Fy1, Tz1, Fx3 and Fy3 are identified as almost perfectly classically damped, while some scatter can be observed in the remaining modes, particularly in mode Fy2.

Table 1: Input parameters of the modal identification methods used in the Sciri Tower.

COV-SSI
$[n_{min}, n_{max}] = [40, 80]$, $\Delta n = 1$
$[j_{b,min}, j_{b,max}] = [140, 200]$, $\Delta j_b = 10$
$\zeta_{max} = 10\%$, $s = 5\%$
$\epsilon_f = 0.05$, $\epsilon_\zeta = 0.01$, and $\epsilon_{MAC} = 0.01$
ERA
$[n_{min}, n_{max}] = [40, 80]$, $\Delta n = 1$
$[j_{b,min}, j_{b,max}] = [100, 160]$, $\Delta j_b = 10$
$\zeta_{max} = 10\%$, $s = 5\%$
$\epsilon_f = 0.05$, $\epsilon_\zeta = 0.01$, and $\epsilon_{MAC} = 0.01$
p-LSCF
$[n_{min}, n_{max}] = [200, 300]$, $\Delta n = 1$
Cross half-spectra by the Welch's method:
2^{13} data points with 50% overlap
EFDD
Spectral density matrix by the Welch's method:
2^{11} data points with 50% overlap
Single-Input-Single-Output (SISO) version of the
Ibrahim Time Domain (ITD) method

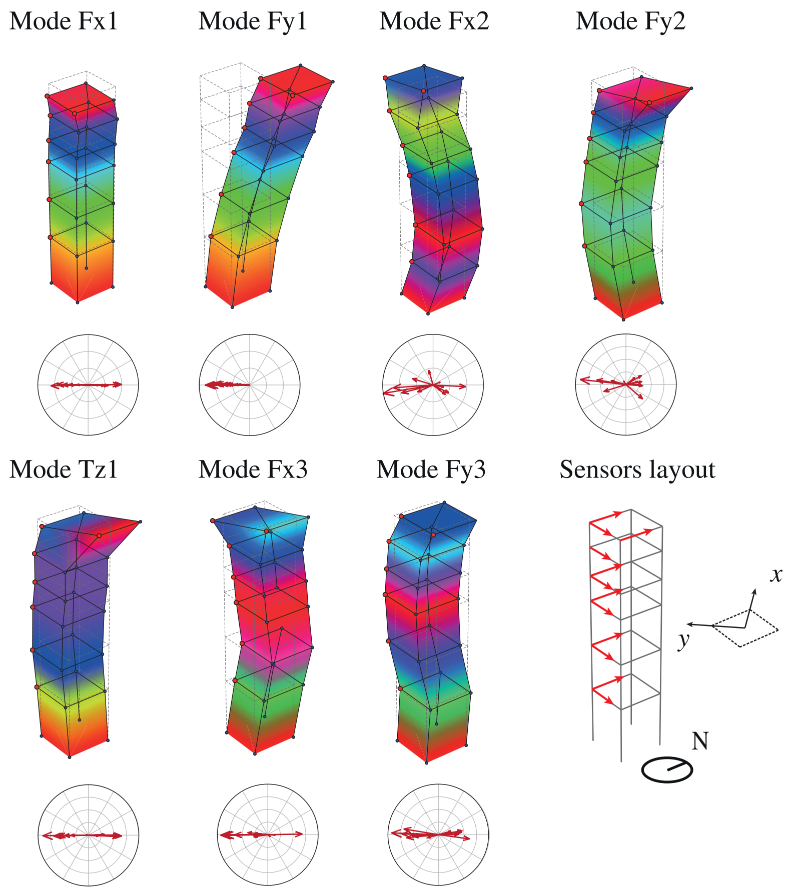

Figure 3: Experimentally identified mode shapes estimated through COV-SSI on February 13th 2019 at 14:00 UTC.

Table 2: Experimentally identified natural frequencies, f_i, and damping ratios, ζ_i, using the COV-SSI, ERA, p-LSCF and EFDD methods on February 13th 2019 at 2:00 pm.

	COV-SSI		ERA		p-LSCF		EFDD	
Mode	f_i^{exp} [Hz]	ζ_i [%]	f_i^{exp} [Hz]	ζ_i [%]	f_i^{exp} [Hz]	ζ_i [%]	f_i^{exp} [Hz]	ζ_i [%]
Fx1	1.692	0.921	1.691	0.838	1.691	0.622	1.691	0.819
Fy1	1.891	0.767	1.890	0.791	1.891	0.559	1.888	0.751
Fx2	5.447	5.002	5.440	5.547	5.531	0.749	5.476	0.605
Fy2	5.819	2.044	5.822	2.114	5.846	0.211	5.810	-
Tz1	8.206	1.787	8.212	1.938	8.190	0.725	8.159	-
Fx3	9.789	1.333	9.789	1.446	9.796	-	9.740	-
Fy3	10.824	3.134	10.858	3.410	10.770	-	-	-

3.3. Continuous OMA of the Sciri Tower

The vibrational modes of the Sciri Tower previously presented in Fig. 3 and Table 2 have been continuously identified and tracked by the COV-SSI method throughout the monitoring period. To do so, the 30-min long vibration records have been down-sampled to 40 Hz, and the modal features have been extracted using the automated OMA procedure previously introduced in Section 3.1. Figure 4 shows the time histories of the natural frequencies of the first seven modes of the tower continuously identified and tracked throughout the monitoring period since February 13th until March 10th 2019. In this figure, the temperature time series recorded by the two thermocouples (indoor and outdoor) are also shown. Clear day-night oscillations can be found in all the natural frequencies, with increases during daytime and decreases during night-time. Figure 5 further investigates the effects of environmental temperature on the resonant frequencies of the tower. It is noted that there is a positive correlation of all the frequencies with temperature, that is, increasing temperatures yield increasing natural frequencies and vice versa. Such a behaviour is often found in historic structures, where the thermal expansion of masonry originates the closure of superficial cracks or micro-cracks, as well as minor discontinuities in the structure [42]. Finally, it is observed that the thermal sensitivity of the resonant frequencies, given by the slope of the linear fittings included in Fig. 5, is larger for higher-order modes.

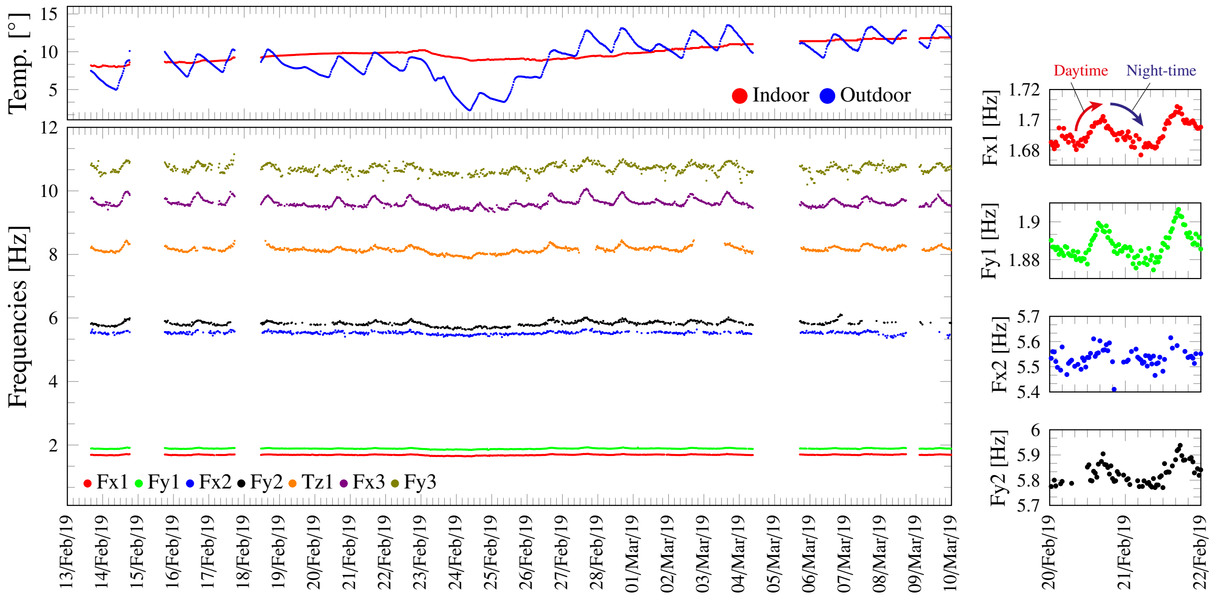

Figure 4: Temperature time series and frequency tracking in the Sciri Tower since February 13th until March 10th 2019.

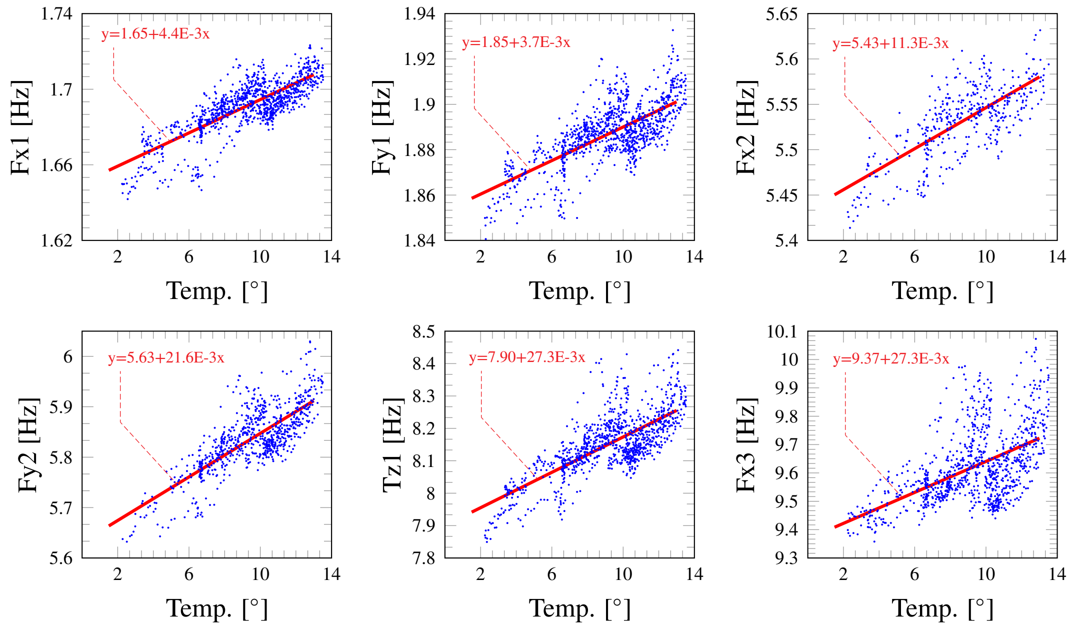

Figure 5: Identified natural frequencies versus outdoor temperature.

4. Automated Ambient Noise Deconvolution Interferometry

This section reports the results of the wave propagation analyses conducted in the Sciri Tower by ANDI. Seismic interferometry is based upon the assessment of travelling pulses and the spatial distribution of their velocity by means of the analysis of transfer functions (TFs). A transfer function $\widehat{h}(z,\omega)$ can be defined as the deconvolution of a reference input signal $u(z_{ref},\omega)$ recorded at a reference station z_{ref} with an output signal $u(z,\omega)$ recorded at an arbitrary station z, and is typically computed in the angular frequency domain ω as [20, 22, 43]:

$$\widehat{h}(z,\omega) = \frac{u(z,\omega)\,\overline{u(z_{ref},\omega)}}{\left|u(z_{ref},\omega)\right|^2 + \epsilon}, \tag{6}$$

where the bar indicates complex conjugate, and ϵ denotes a regularization parameter used to avoid numerical instability due to division by small numbers. In this work, ϵ has been set to 10% of the average power spectrum of the reference input signal. According to Eq. (6), $u(z,\omega)$ represents the Fourier transform of the time domain signal, $U(z,t)$, that may for instance represent a displacement, velocity or acceleration component along a certain direction at height. The transformation of $\widehat{h}(z,\omega)$ to the time domain t represents the IRF, $h(z,t)$, between the output and input signals. The IRF constitutes the Green's function of the system and characterizes the propagation of a Dirac Delta impulse applied at the reference station. Given that the signals are discretely sampled at a certain sampling frequency F_s, the IRFs can be computed by taking the inverse Fourier transform of the corresponding TFs as follows:

$$h(z,t) = \frac{1}{2\pi}\int_{-\omega_{max}}^{+\omega_{max}} \widehat{h}(z,\omega)e^{-\mathrm{i}\omega t}\,\mathrm{d}\omega, \tag{7}$$

with $\omega_{max} = (F_s/2)/2\pi$ and i being the imaginary unit. These functions provide a representation of the propagating waveforms in the building, and their velocity distribution can be obtained by simple peak-picking analysis of IRFs computed at different heights. To this end, the time-lag τ_i between the motions recorded at two different levels z_{i+1} and z_i is obtained by peak-picking the maxima of the IRFs $h(z_{i+1},t)$ and $h(z_i,t)$ along an identified ray path [20]. Then, the velocity of the pulses can be computed as $v_i = l_i/\tau_i$, with l_i being the separation between the stations $l_i = z_{i+1} - z_i$. Note that the number of IRFs that can be computed in a building monitored at N different levels equals N and, therefore, the resolution of the shear wave distribution is $N-1$. The integration of ANDI alongside the automated OMA of the Sciri tower is sketched in Fig. 2.

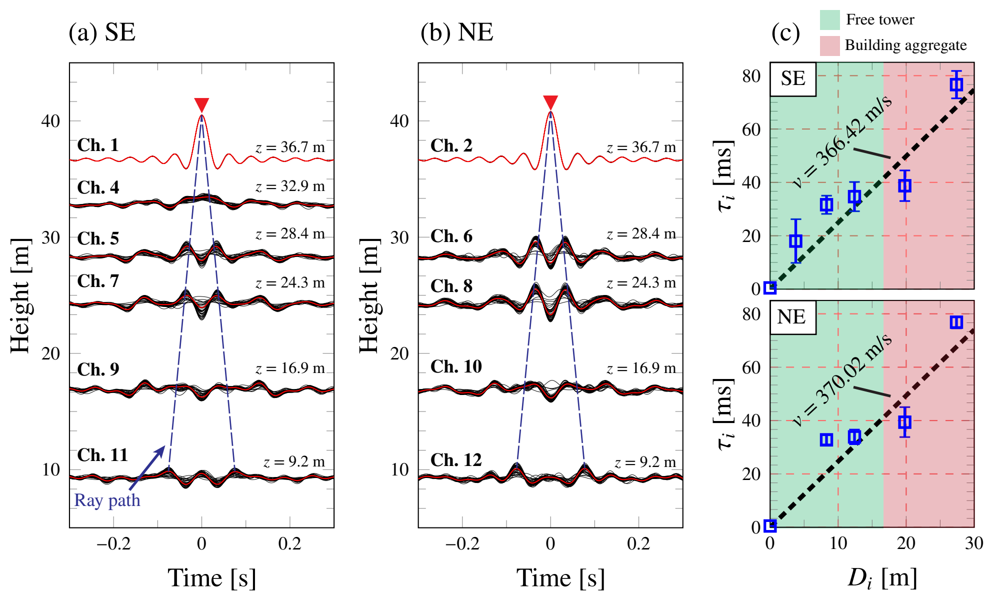

Figure 6: Staking waveforms over 30-min intervals of the IRFs for the first 48 hours and filtered in the broad-band frequency of 0.1-20 Hz, (a) NE component, and (b) SE component. The red lines indicate the staked IRFs over the first 48 hours. (c) Travel times at different heights versus distance to the roof. The error bars denote the standard deviations of the travel times obtained for every 30-min long records, and the global velocity of the waves crossing the whole structure is denoted with black dashed lines and is computed using a least squares fit (F_s=200 Hz).

Table 3: Mean $\overline{\tau_i}$ and standard deviation values of the wave arrival times obtained by peak-picking analysis of the IRFs staked over 30-min intervals throughout the first 48 hours (0.1-20 Hz, 10-min-long time windows with 50% overlap).

		Direction: SE (Channels 1, 4, 5, 7, 9, and 11)								
		F_s=200 Hz			F_s=1000 Hz			F_s=5000 Hz		
z [m]	D_i [m]	$\overline{\tau_i}$ [ms]	σ_τ [ms]	v [m/s]	$\overline{\tau_i}$ [ms]	σ_τ [ms]	v [m/s]	$\overline{\tau_i}$ [ms]	σ_τ [ms]	v [m/s]
36.70	0.00	0.500	0.000		1.502	0.000		0.100	0.000	
32.90	3.80	18.021	8.189		20.634	7.499		24.987	6.696	
28.40	8.30	31.608	3.416		32.151	2.239		32.600	1.534	
24.30	12.40	34.671	5.487	301.144	33.405	3.640	294.651	32.993	5.067	294.779
16.90	19.80	38.750	5.736		38.048	7.429		35.154	6.672	
9.30	27.40	76.634	5.138	388.785	73.419	3.788	404.363	73.974	3.305	405.171

		Direction: NE (Channels 2, 6, 8, 10 and 12)								
		F_s=200 Hz			F_s=1000 Hz			F_s=5000 Hz		
z [m]	D_i [m]	$\overline{\tau_i}$ [ms]	σ_τ [ms]	v [m/s]	$\overline{\tau_i}$ [ms]	σ_τ [ms]	v [m/s]	$\overline{\tau_i}$ [ms]	σ_τ [ms]	v [m/s]
36.70	0.00	0.500	0.000		1.502	0.000		0.100	0.000	
28.40	8.30	32.779	1.725		32.414	2.087		33.409	1.537	
24.30	12.40	33.877	2.737	311.442	33.420	2.159	314.978	33.953	2.021	307.762
16.90	19.80	39.420	5.611		39.534	6.551		38.936	5.983	
9.30	27.40	76.706	2.153	387.518	76.824	2.131	386.844	77.544	2.022	384.594

Based upon the previously outlined theoretical framework, ANDI has been applied to every 30-min ambient vibration records, and the arrival times of the travelling pulses have been automatically identified and tracked. In order to minimize the variance of the estimates of the wave velocities, the IRFs have been computed considering 10-min-long windows with 50% overlap and staked (averaged) over every 30-min long vibration record. In addition, virtual sources have been considered at the roof level (z_{ref} = 36.70 m), and the resulting waveforms have been filtered to the frequency band 0.1-20 Hz. Figures 6 (a) and (b) show the IRFs in the SE (Channels 1, 4, 5, 7, 9, and 11) and NE (Channels 2, 6, 8, 10 and 12) directions, respectively, obtained for every 30-min-long ambient vibration recorded during the first 48 hours and sampled at F_s=200 Hz. It is noted in these figures that two quasi-symmetric pulses can be clearly identified (with ray paths denoted by blue dashed lines), so that wave velocities have been computed as the average of the upward and downward pulses. By means of the peak-picking analysis of these IRFs, Fig. 6 (c) depicts the computed wave travel times τ_i versus the distance D_i from the reference level z_{ref} = 36.7 m. The error bars in the graph represent the standard deviations of the computed wave arrival times, and the global wave velocities (velocity of the waves to cross the whole tower) are represented with black dashed lines. These are computed using a least squares fitting of the arrival times obtained from the staked IRFs throughout the first 48 hours. In order to deepen into this analysis, Table 3 collects the mean $\overline{\tau_i}$ and standard deviation values σ_τ of the wave arrival times obtained by peak-picking analysis of the IRFs staked over 30-min intervals throughout the first 48 hours, considering sampling frequencies of F_s = 200 Hz, F_s = 1000 Hz, and F_s = 5000 Hz. Moreover, shear S-wave velocities in the heights of 24.3-36.70 m and 9.3-24.3 m computed by least squares fitting of the mean arrival times are also reported, representing the velocities of the sections of the structure of free tower and constrained by the adjoining building, respectively. Firstly, it is noted that the wave velocity is larger in all the cases in the bottom part of the tower because of the contribution of the building aggregate. Furthermore, the velocity of the bottom part is lower in the NE direction where one of the façades of the tower remains unrestrained (see Fig. 1). Conversely, the velocity of the uppermost part of the tower is always larger in the NE direction, where so is its inertia and thus its stiffness. Therefore, these results evidence the potential of ANDI to represent well the physics underlying the dynamic response of structures. The study of the effects of the sampling frequency is completed in the analyses reported hereafter.

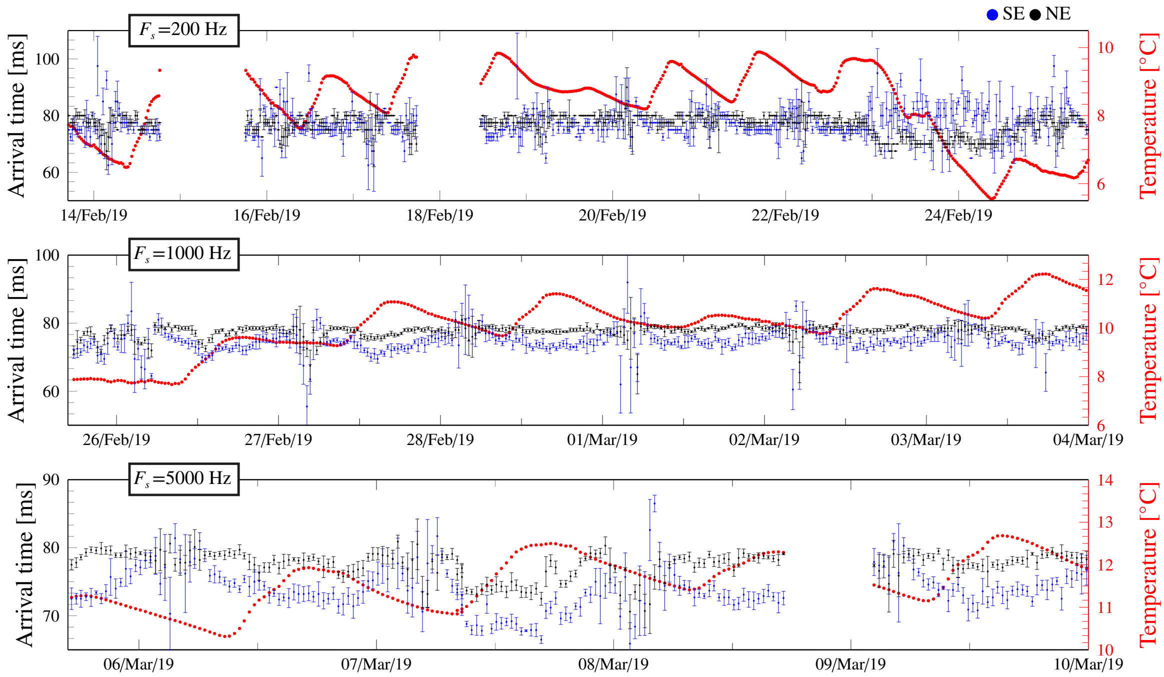

Figure 7: Time series of wave arrival times in the NE and SE directions of the Sciri Tower since February 13th until March 10th 2019. Error bars indicate the standard deviation of the identified arrival times obtained by every 10-min-long windows stacked over every 30-min vibration record.

Figure 7 shows the time series of the identified wave arrival times in the NE and SE directions of the Sciri Tower considering sampling frequencies of 200 Hz (Feb. 13th - Feb. 25th 2019), 1000 Hz (Feb. 24th - Mar. 4th 2019), and 5000 Hz (Mar. 4th - Mar. 10th 2019). Error bars indicate the standard deviation of the arrival times obtained from every 10-min-long window stacked over every 30-min vibration record. It is first noted that, while some day-night fluctuations are effectively captured, a considerable scatter is found in the wave arrival times obtained with a sampling frequency of 200 Hz. This fact raises one of the most challenging issues of this technology, that is the need for high sampling frequencies for an accurate assessment of the velocity of propagating waves. As evidenced by the results of Lacanna *et al.* [36], the high velocity of travelling pulses, along with the limited separation between sensors that is typically possible in historic buildings, make the detection of environmental effects require high sampling frequencies. In addition, the effects of early-stage damage are usually lower than environmental effects (see e.g. [14, 38]), thereby high-sampling frequencies are critical for early damage detection in ANDI-based SHM systems. In particular, for a given wave velocity c and separation l between sensors, i.e. a wave lag $\tau = l/c$, a rough estimate of the relationship between the minimum observable reductions in the wave velocity δc and the sampling frequency F_s reads:

$$\delta c = -\frac{l}{F_s \tau^2 + \tau}. \tag{8}$$

Considering a wave velocity of 366.42 m/s, as obtained in Fig. 6 (c) in the SE direction, and a maximum sensor separation of 27.4 m, the maximum observable reduction in the wave velocity considering a sampling frequency of 200 Hz ($\Delta t = 5$ ms) is 23 m/s. On the other hand, the minimum observable velocity variations are 5 m/s and 1 m/s for sampling frequencies of 1000 Hz ($\Delta t = 1$ ms) and 5000 Hz ($\Delta t = 0.2$ ms), respectively. The resolution of the identified wave velocities is inversely proportional to the separation of the sensors as shown in Eq. (8), therefore the need for high sampling frequencies increases for the assessment of local wave velocities and their profile along the tower. In this regard, a clearer representation of day/night fluctuations can be noted for increasing sampling frequencies in Fig. 6. Specifically, it is observed in all the cases that wave arrival times decrease for increasing environmental temperature. Alternatively, wave velocities (i.e. stiffness) increase for increasing temperature. These results agree with the previously reported results on the day/night fluctuations of the resonant frequencies in Fig. 4 as a result of temperature-induced closure of cracks. With regard to the uncertainty in the tracking of the wave arrival times, it is noted in Fig. 7 that the standard deviations increase systematically between 1:00 and 5:00 a.m. This fact indicates limitations in the identification stemming from low signal-to-noise ratio since ambient excitation due to traffic and human activities is minimum during this time lapse. For more comprehensive information on the limitations and implications of the input parameters in the wave identification of slender structures with beam-like dynamic behaviour (e.g. towers, and high-rise buildings), readers may refer to reference [37].

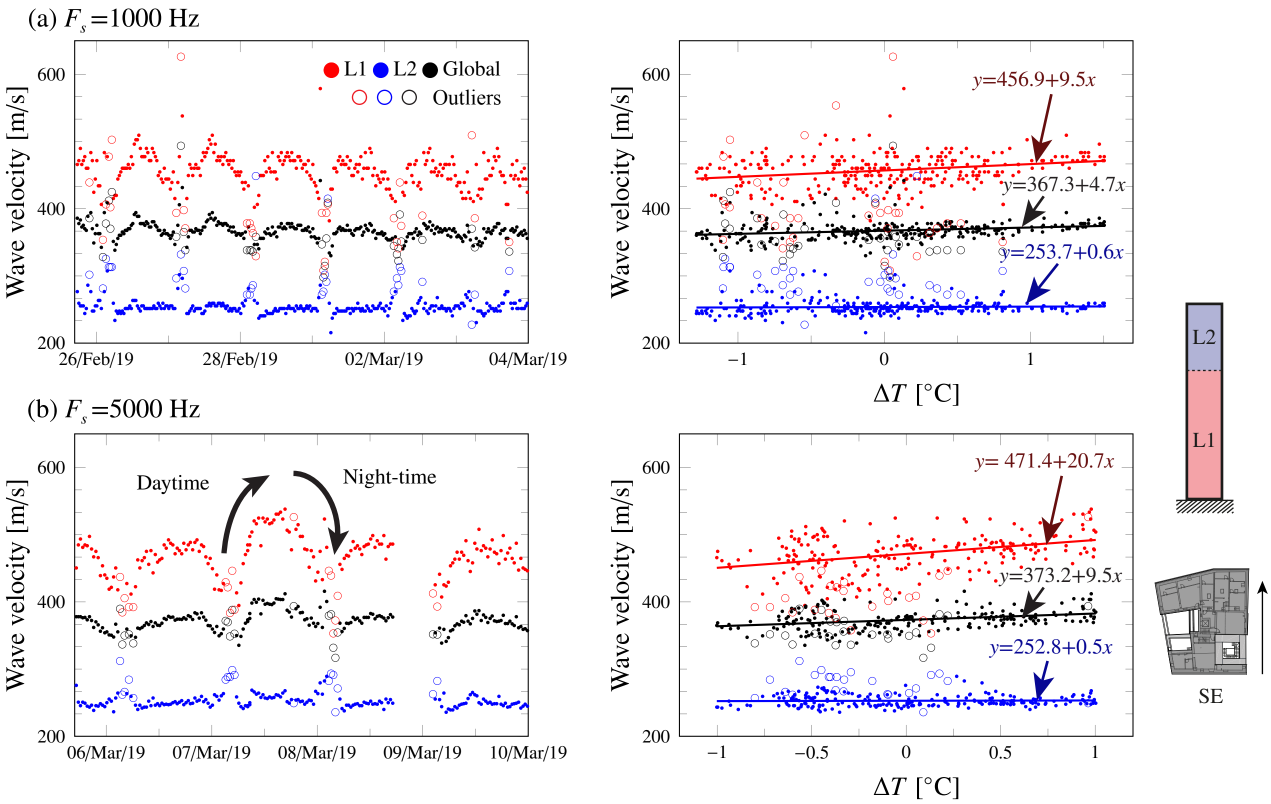

Figure 8: Wave velocity tracking in the SE direction of the Sciri tower considering two layers, L1 (9.3 m< z <28.4 m), and L2 (28.4 m< z <36.7 m), and the whole tower (9.3 m< z <36.7 m), with sampling frequencies of F_s=1000 Hz and 5000 Hz.

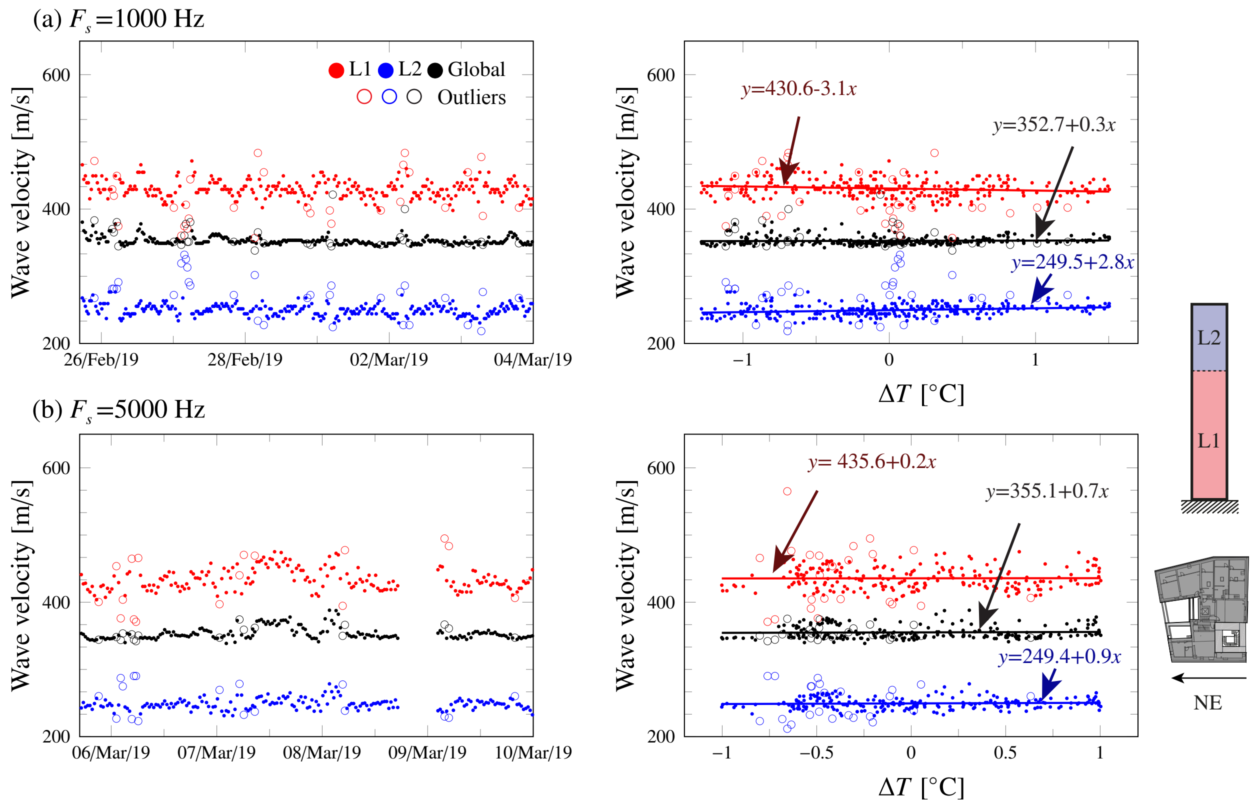

Figure 9: Wave velocity tracking in the NE direction of the Sciri tower considering two layers, L1 (9.3 m< z <28.4 m), and L2 (28.4 m< z <36.7 m), and the whole tower (9.3 m< z <36.7 m), with sampling frequencies of F_s=1000 Hz and 5000 Hz.

Larger temperature sensitivities in the SE direction of the Sciri Tower can be visually observed in Fig. 7. In order to further investigate these effects, Figs. 8 and 9 depict the identified wave velocities in the SE and NE directions versus environmental temperature, respectively. Furthermore, in order to assess the potential of this approach for identifying local wave velocities, two different layers are considered, namely L1 (9.3 m< z <28.4 m), and L2 (28.4 m< z <36.7 m). In these analyses, only the results obtained for sampling frequencies of 1000 Hz and 5000 Hz are presented, since the accuracy of the identification performed with 200 Hz has proved insufficient to capture temperature-induced daily fluctuations. In order to extract robust correlations between wave velocities and environmental temperature, the corrupted wave identification results during the early morning hours due to low excitation levels have been filtered out using the Minimum Covariance Determinant (MCD) method [44]. The MCD method seeks a sample subset within a multivariate dataset (in this work the tracked wave velocities in L1, L2, and the whole tower) that minimize the covariance matrix. Specifically, we have sought a subset of $\approx 0.9 n_p$ samples, with n_p being the number of data points in the time series of identified wave velocities. Then, the 10% of the samples in the time series of velocities with the largest Mahalanobis distances with respect to the previously defined sample subset are selected as outliers. On this basis, the correlations indicated in Figs. 8 and 9 have been obtained disregarding the identified outliers (data points denoted with empty circle markers).

In general, it can be concluded from Figs. 8 and 9 that the relation between wave velocities and environmental temperature can be approximately defined as linear. It is observed that the accuracy of the identification considerably improves with the sampling frequency of 5000 Hz, while many outliers are present in the results obtained for F_s = 1000 Hz due to poor sampling limitations in the peak-picking analysis. It is also interesting to note that, in both cases, wave velocities are larger in the bottom layer L1 where the contribution of the building aggregate is localized. With regard to the effects of environmental temperature, it is noted that global velocities exhibit positive correlations with temperature, and the sensitivity in the SE direction (F_s = 5000 Hz, 9.5 m/s/C°) is substantially larger than in the NE direction (F_s = 5000 Hz, 0.7 m/s/C°). Considering the plan distribution of the building ensemble, such a behaviour is reasonable given that the horizontal constraint imposed by the aggregate is stronger in the SE direction. In terms of local velocities, some differences can be noted in the SE and NE directions. In the SE direction, a large positive correlation (F_s = 5000 Hz, 20.7 m/s/C°) between wave velocity and environmental temperature is found in the bottom layer L1. This behaviour is ascribed to larger temperature-induced crack closure effects in the section of the tower constrained by the building aggregate, where thermal expansion is more constrained and the heterogeneity degree of the material is larger. Conversely, a small correlation (F_s = 5000 Hz, 0.5 m/s/C°) is found in the top section of the tower (L2) where thermal expansion is minimally constrained. In the NE direction, small temperature sensitivities are found in both layers, and with opposite sign to those obtained in the SE direction. These results evidence the key role of the building aggregate into the effects of environmental temperature on the stiffness distribution of the Sciri Tower.

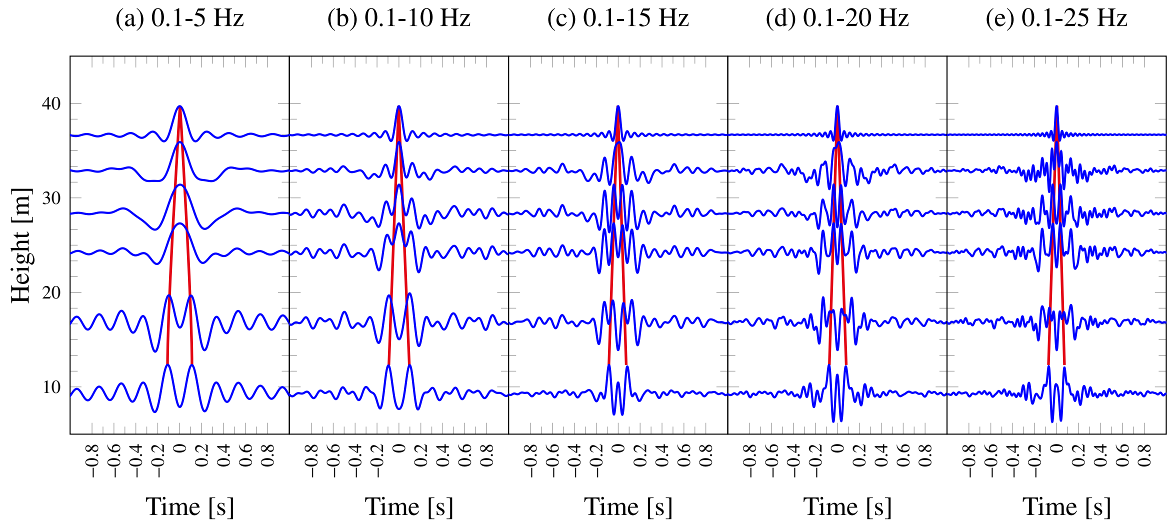

Figure 10: Band-pass filtered ($f_1 - f_2$) IRFs staked over the first 48 hours in the SE direction of the Sciri Tower considering different frequency bands (F_s = 200 Hz).

Table 4: Wave velocities obtained by peak-picking analysis of band-pass filtered ($f_1 - f_2$) IRFs staked over the first 48 hours in the SE direction of the Sciri Tower considering different frequency bands (f_1 = 0.1 Hz, F_s = 200 Hz).

f_2 [Hz]	v [m/s]	$\Delta v/\Delta f_2$ [m/s/Hz]
5	185.57	
10	212.22	26.65
15	228.37	16.16
20	282.86	54.48
25	304.62	21.76

As stated earlier in the introduction, high-rise buildings such as towers have been reported in the literature to often exhibit a dispersive behaviour [28]. This is characterized by the variation of the wavenumber k or, alternatively, the velocity of the propagating waves, as a function of frequency ω according to a certain dispersion relation. More specifically, wavefronts can be defined by phase and group velocities as $c^{ph} = \omega/k$ and $c^{gr} = \partial\omega/\partial k$, respectively. The phase velocity determines the velocity of propagation of the pulses, while the group velocity defines the velocity of the envelopes of the waveforms. When the system is not dispersive, the phase and group velocities coincide, i.e. $c^{ph} = c^{gr}$. It follows that, when the dynamic structural behaviour is dispersive, the characterization of the dispersion curves offers a more convenient way of detecting structural pathologies since they cover the main range of operating frequencies, instead of simply assessing discrete frequency ranges where damage-induced structural changes may go unnoticed. In order to investigate the dispersion properties of the Sciri Tower, ANDI has been performed considering different frequency bands with higher cut-off frequencies, namely 5 Hz, 10 Hz, 15 Hz, 20 Hz and 25 Hz, and the IRFs have been stacked over the first 48 hours. The resulting IRFs are shown in Fig. 10, and the wave velocities obtained by peak-picking analysis are collected in Table 4. It is noted that, effectively, the wave velocities increase for higher frequencies, which evidences a dispersive-type behaviour. In order to further analyse the variation of wave velocities with frequency, the relative variations of the identified wave velocities with the upper cut-off frequency ($\Delta v/\Delta f_2$) are also reported in Table 4. It is interesting to note that the variation rates experience a large increase between cut-off frequencies of 15 and 20 Hz.

The analysis of dispersion has been deepened by means of the multi-channel analysis of surface waves (MASW) method developed by Park et al. [45]. The MASW method conceives the IRF traces $h(z, \omega)$ as the multiplication of two separate terms:

$$h(z, \omega) = \mathrm{e}^{-\mathrm{i}kz} A(z, \omega), \tag{9}$$

where $A(z,\omega)$ is an amplitude spectrum and contains the information about attenuation, spherical divergence and source spectrum characteristics. Since the amplitude does not contain any information linked to the phase velocity, the following integral transformation is applied to $h(z,\omega)$:

$$V(\omega,\phi) = \int e^{i\phi z}\left[h(z,\omega)/\left|h(z,\omega)\right|\right] dz = \int e^{-i(k-\phi)z}\left[A(z,\omega)/\left|A(z,\omega)\right|\right] dz. \tag{10}$$

Such an integral transform can be understood as the sum over offset of wavefields of a frequency after applying offset-dependent phase shifts defined by assuming a phase velocity $c^{ph} = \omega/\phi$. Therefore, for a given frequency ω, $V(\omega,\phi)$ presents a maximum if $\phi = k$. Dispersion images can be extracted by considering a discrete sampling of the frequency range of interest, as well as of the search space of phase velocities, and mapping the values of $V(\omega,\phi)$ in a 2D format (i.e., phase velocity $c^{ph} = \omega/\phi$ versus frequency ω). In this bi-dimensional graph, dispersion curves can be traced by following the peaks along the frequency axis.

The previously outlined MASW method has been applied to the ambient vibrations recorded in the Sciri Tower along the SE direction and the results are shown in Fig. 11. To do so, wave velocities between 50 and 2000 m/s have been scanned with a velocity step of 1 m/s, and frequencies between 1 and 50 Hz have been sampled every 0.33 Hz. The analysis has been performed considering 3 s long IRFs (-1.5 s< t <1.5 s) obtained with a sampling frequency of 200 Hz and staked over the first 48 hours. In order to take into account the inherent limitations of the sensor array to characterize the dispersion properties, theoretical bounds have been included in Fig. 11 (yellow dashed lines). According to the work of Cornou et al. [46], these correspond to the range of acceptable wavelengths λ given by $\lambda_{min} \leq \lambda \leq \lambda_{max}$, with $\lambda_{min} = 2d$ being the spatial aliasing limit, and $\lambda_{max} = 3D$ the maximum capability of the sensor array to separate two waves propagating at closely spaced wavenumbers, and $d = 3.8$ m and $D = 27.4$ m the minimum and maximum inter-station distances, respectively. Additionally, the wave velocities previously computed by peak-picking analysis in Table 4 have been also included herein. It is noted that the wave velocities estimated by peak-picking analysis follow the first region of peaks of $V(\omega, c^{ph})$. Nevertheless, there is a second region of large $V(\omega, c^{ph})$ values for frequency values above approximately 17 Hz that cannot be explained by peak-picking analysis, what may evidence the presence of a second wave propagation mode. In fact, the change in the variation rates of the wave velocities previously reported in Table 4 between 15 and 20 Hz may be indicative of a bias towards this second propagation mode.

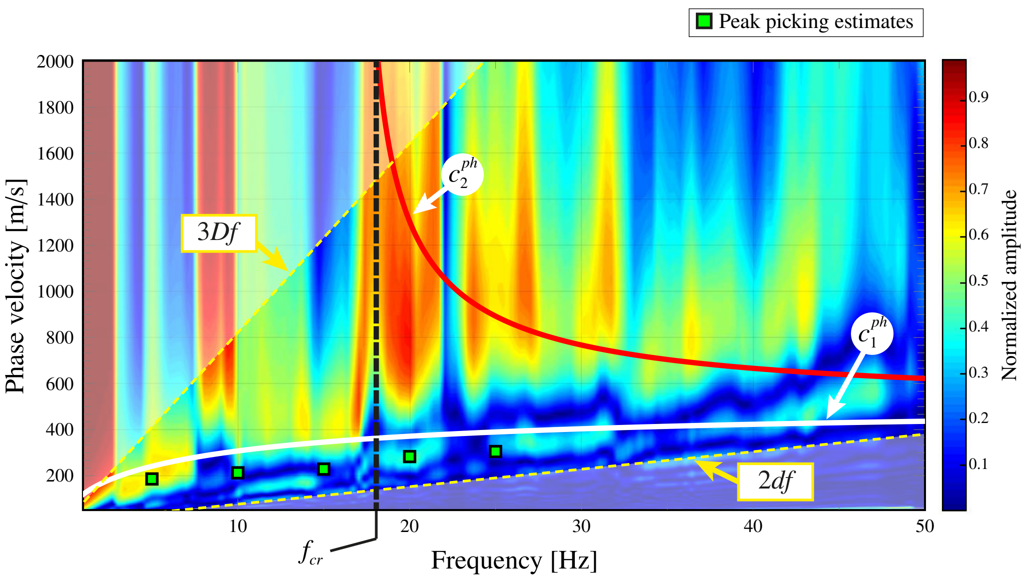

Figure 11: Frequency-phase velocity image of the Sciri Tower in the SE direction (F_s = 200 Hz).

In order to gain a better understanding of the dispersion image previously shown in Fig. 11, the equivalent Timoshenko beam model derived by Ebrahimian and Todorovska [28] is adopted herein. Assuming a building with elastic Young's modulus E, shear modulus G, radius of gyration r_g, shear correction factor k_s, and mass density ρ, those authors demonstrated that waves propagate according to two different propagation modes with phase velocities:

$$c_1^{ph} = c_S \sqrt{2}\left[\left(\frac{1}{k_s} + R\right) + \sqrt{\left(\frac{1}{k_s} - R\right)^2 + \frac{4R}{\Omega^2}}\right]^{-1/2}, \tag{11}$$

$$c_2^{ph} = c_S \sqrt{2}\left[\left(\frac{1}{k_s} + R\right) - \sqrt{\left(\frac{1}{k_s} - R\right)^2 + \frac{4R}{\Omega^2}}\right]^{-1/2}, \tag{12}$$

where $\Omega = \omega r_g / c_S$ and $R = G/E$ are non-dimensional parameters, and $c_L = \sqrt{E/\rho}$ and $c_S = \sqrt{G/\rho}$ are the longitudinal and shear wave velocities in the material, respectively. A closer inspection of Eqs. (11) and (12) reveals that c_1^{ph} is real-valued for all ω, while c_2^{ph} only becomes real when $\omega > \omega_{cr}$, with ω_{cr} being a cut-off frequency for the second wave propagation mode or critical frequency given by [28]:

$$\omega_{cr} = c_S \sqrt{k_s}/r_g. \tag{13}$$

When $\omega < \omega_{cr}$, c_2^{ph} is complex-valued, and the second propagation mode only defines exponentially attenuated non-propagating waves or evanescent waves. Additionally, an asymptotic analysis of Eqs. (11) and (12) shows that when $R \leq 1/k_s$, as it is typically the case, $\lim_{\omega\to\infty} c_1^{ph} = c_S \sqrt{k_s}$ and $\lim_{\omega\to\infty} c_2^{ph} = c_S / \sqrt{R}$. Therefore, the theoretical dispersion curves of the two propagation modes can be obtained by considering a critical frequency value of $f_{cr} = \omega_{cr}/2\pi = 17$ Hz, and the limits $\lim_{\omega\to\infty} c_1^{ph}$=500 m/s and $\lim_{\omega\to\infty} c_2^{ph}$=510 m/s, according to the image dispersion shown in Fig. 11. Moreover, a shear correction factor $k_s = 0.43$ has been also assumed, corresponding to a tower with thin-walled hollow square cross-section according to Cowper's formulae (with Poisson's ratio $\nu = 0.25$) [47]. These assumptions completely define the dispersion curves from Eqs. (11) and (12), and the results have been included in Fig. 11. It is interesting to note that, effectively, the curve corresponding to the second wave propagation mode c_2^{ph} explains the second trend of maximum $V(\omega, c^{ph})$ values. Likewise, the coexistence of these two wave propagation modes above the critical frequency f_{cr} originates complex interference patters, what explains the complex wavefronts previously reported in Figs. (10) (d) and (e). Finally, it should be noted that some differences can be found between the experimental and theoretical dispersion at high frequencies. While the analytical solution for c_2^{ph} reports monotonically decreasing values, the experimental dispersion image yields peaks with increasing phase velocities for increasing frequencies. This fact may evidence modelling limitations of the TB model developed by Ebrahimian and Todorovska [28] for this case study, and the contribution of the building aggregate may require more sophisticated modelling approaches for explaining the dispersion behaviour of the Sciri Tower for high frequency bands.

5. Conclusions

This paper has proposed the coupled application of automated OMA and ANDI for the full structural system identification of historic structures. The Sciri Tower in Perugia (Italy) has been presented as a validation case study to evaluate the effectiveness of the proposed methodology for identifying environmental effects. To do so, a vibration-based monitoring system consisting of twelve accelerometers deployed at different heights of the tower have been installed, and ambient vibrations have been recorded since February 13th until March 10th 2019. The presented results report the identification and tracking of the modal properties and wave propagation properties of the Sciri Tower throughout the monitoring time. In order to assess the robustness of the identification of ambient noise waves, three different sampling frequencies have been used in the monitoring, including $F_s = 200$ Hz, 1000 Hz, and 5000 Hz. The results have highlighted the importance of high sampling frequencies for detecting the influence of environmental temperature and, as a result, for SHM systems for early damage detection. In addition, ANDI has proved to represent a complementary technique to OMA, and its capability for providing local information on the intrinsic stiffness properties of the Sciri Tower has been shown. Finally, the reported results have shed some light into the dispersion effects on the wave propagation properties of the tower.

The main key findings of this research can be summarised as follows:

- High sampling frequencies have been shown crucial for detecting environmental effects on wave velocities. Specifically, a positive correlation between wave velocities and environmental temperature has been found by using sampling frequencies of 1000 Hz and 5000 Hz. This behaviour has been ascribed to temperature-induced closure of cracks and discontinuities, and is consistent with the observed positive correlation between resonant frequencies and environmental temperature of seven vibration modes identified and tracked in the frequency interval 0-12 Hz.

- Wave velocities obtained by peak-picking analysis of IRFs have proved to provide valuable information about the stiffness distribution of the Sciri Tower. In particular, increasing wave velocities have been found in height, and local analyses have allowed us to identify the constraints imposed by the adjoining building in two orthogonal directions.
- The presented results have shown that, in the SE direction (direction of maximum constraint by the adjoining building), the bottom part of the tower is highly sensitive to temperature fluctuations. Conversely, motions in the NE direction (direction with one of the façades of the tower unconstrained by the building aggregate) are minimally affected by temperature. This behaviour is conceivably associated to the circumstance that temperature-induced deformation is more constrained in the lower part of the tower.
- Peak-picking analyses of band-pass filtered IRFs have evidenced the dispersion-type behaviour of the Sciri tower. Additionally, dispersion imaging techniques have been applied and compared to theoretical results reported by an equivalent Timoshenko beam model. The results have evidenced the presence of two different wave propagation modes above a critical frequency of $f_{cr} \approx 17$ Hz. Therefore, in application to masonry towers, it is recommended to filter the IRFs obtained by ANDI below f_{cr} to avoid complex interference patterns between two propagating modes, with f_{cr} being possibly estimated as in Eq. (13).

Acknowledgement

This work was supported by the Italian Ministry of Education, University and Research (MIUR) through the funded project of national interest “DETECT-AGING - Degradation Effects on sTructural safEty of Cultural heriTAGe constructions through simulation and health monitorING” (Protocol No. 201747Y73L).

References

References

[1] C. Gentile, G. Bernardini, Output-only modal identification of a reinforced concrete bridge from radar-based measurements, NDT & E International 41 (2008) 544–553.

[2] W. Fan, P. Qiao, Vibration-based damage identification methods: a review and comparative study, Structural Health Monitoring 10 (2011) 83–111.

[3] E. Reynders, System identification methods for (operational) modal analysis: review and comparison, Archives of Computational Methods in Engineering 19 (2012) 51–124.

[4] E. P. Carden, P. Fanning, Vibration based condition monitoring: a review, Structural health monitoring 3 (2004) 355–377.

[5] S. K. Au, F. L. Zhang, Y. C. Ni, Bayesian operational modal analysis: theory, computation, practice, Computers & Structures 126 (2013) 3–14.

[6] M. G. Masciotta, L. F. Ramos, P. B. Lourenço, The importance of structural monitoring as a diagnosis and control tool in the restoration process of heritage structures: a case study in Portugal, Journal of Cultural Heritage 27 (2017) 36–47.

[7] X. Kong, J. Li, W. Collins, C. Bennett, S. Laflamme, H. Jo, Sensing distortion-induced fatigue cracks in steel bridges with capacitive skin sensor arrays, Smart Materials and Structures 27 (2018) 115008.

[8] R. M. Azzara, G. De Roeck, M. Girardi, C. Padovani, D. Pellegrini, E. Reynders, The influence of environmental parameters on the dynamic behaviour of the San Frediano bell tower in Lucca, Engineering Structures 156 (2018) 175–187.

[9] E. Mesquita, A. Arêde, N. Pinto, P. Antunes, H. Varum, Long-term monitoring of a damaged historic structure using a wireless sensor network, Engineering Structures 161 (2018) 108–117.

[10] P. Pachón, R. Castro, E. García-Macías, V. Compan, E. Puertas, E. Torroja’s bridge: Tailored experimental setup for SHM of a historical bridge with a reduced number of sensors, Engineering Structures 162 (2018) 11–21.

[11] S. Ivorra, D. Foti, V. Gallo, V. Vacca, D. Bru, Bell’s dynamic interaction on a reinforced concrete bell tower, Engineering Structures 183 (2019) 965–975.

[12] C. Gentile, C. Poggi, A. Ruccolo, M. Vasic, Vibration-Based Assessment of the Tensile Force in the Tie-Rods of the Milan Cathedral, International Journal of Architectural Heritage (2019) 1–14.

[13] W. Soo Lon Wah, Y. T. Chen, G. W. Roberts, A. Elamin, Separating damage from environmental effects affecting civil structures for near real-time damage detection, Structural Health Monitoring 17 (2018) 850–868.

[14] F. Ubertini, N. Cavalagli, A. Kita, G. Comanducci, Assessment of a monumental masonry bell-tower after 2016 Central Italy seismic sequence by long-term SHM, Bulletin of Earthquake Engineering 16 (2018) 775–801.

[15] E. Şafak, Wave-propagation formulation of seismic response of multistory buildings, Journal of Structural Engineering 125 (1999) 426–437.

[16] M. I. Todorovska, S. S. Ivanović, M. D. Trifunac, Wave propagation in a seven-story reinforced concrete building: I. Theoretical models, Soil Dynamics and Earthquake Engineering 21 (2001) 211–223.

[17] R. Snieder, E. Şafak, Extracting the building response using seismic interferometry: Theory and application to the Millikan Library in Pasadena, California, Bulletin of the Seismological Society of America 96 (2006) 586–598.

[18] M. D. Trifunac, S. S. Ivanović, M. I. Todorovska, Wave propagation in a seven-story reinforced concrete building: III. Damage detection via changes in wavenumbers, Soil Dynamics and Earthquake Engineering 23 (2003) 65–75.

[19] M. D. Kohler, T. H. Heaton, S. C. Bradford, Propagating waves in the steel, moment-frame factor building recorded during earthquakes, Bulletin of the Seismological Society of America 97 (2007) 1334–1345.

[20] M. I. Todorovska, M. T. Rahmani, System identification of buildings by wave travel time analysis and layered shear beam models–Spatial resolution and accuracy, Structural Control and Health Monitoring 20 (2013) 686–702.

[21] S. S. Ivanovic, M. D. Trifunac, M. D. Todorovska, On identification of damage in structures via wave travel times, in: Strong Motion Instrumentation for Civil Engineering Structures, Springer, 2001, pp. 447–467.

[22] M. I. Todorovska, M. D. Trifunac, Earthquake damage detection in the Imperial County Services Building III: analysis of wave travel times via impulse response functions, Soil Dynamics and Earthquake Engineering 28 (2008) 387–404.

[23] M. Rahmani, M. Ebrahimian, M. I. Todorovska, Time-wave velocity analysis for early earthquake damage detection in buildings: Application to a damaged full-scale RC building, Earthquake Engineering & Structural Dynamics 44 (2015) 619–636.

[24] M. Ebrahimian, M. Rahmani, M. I. Todorovska, Nonparametric estimation of wave dispersion in high-rise buildings by seismic interferometry, Earthquake Engineering & Structural Dynamics 43 (2014) 2361–2375.

[25] M. I. Todorovska, Seismic interferometry of a soil-structure interaction model with coupled horizontal and rocking response, Bulletin of the Seismological Society of America 99 (2009) 611–625.

[26] M. I. Todorovska, Soil-structure system identification of Millikan Library North-South response during four earthquakes (1970-2002): What caused the observed wandering of the system frequencies?, Bulletin of the Seismological Society of America 99 (2009) 626–635.

[27] M. Rahmani, M. Ebrahimian, M. I. Todorovska, Wave dispersion in high-rise buildings due to soil–structure interaction, Earthquake Engineering & Structural Dynamics 44 (2015) 317–323.

[28] M. Ebrahimian, M. I. Todorovska, Wave propagation in a Timoshenko beam building model, Journal of Engineering Mechanics 140 (2013) 04014018.

[29] M. I. Todorovska, M. D. Trifunac, Impulse response analysis of the Van Nuys 7-storey hotel during 11 earthquakes and earthquake damage detection, Structural Control and Health Monitoring: The Official Journal of the International Association for Structural Control and Monitoring and of the European Association for the Control of Structures 15 (2008) 90–116.

[30] M. Rahmani, M. I. Todorovska, 1D system identification of buildings during earthquakes by seismic interferometry with waveform inversion of impulse responses–method and application to Millikan library, Soil Dynamics and Earthquake Engineering 47 (2013) 157–174.

[31] M. Ebrahimian, M. I. Todorovska, Structural system identification of buildings by a wave method based on a nonuniform Timoshenko beam model, Journal of Engineering Mechanics 141 (2015) 04015022.

[32] E. García-Macías, F. Ubertini, Seismic interferometry for earthquake-induced damage identification in historic masonry towers, Mechanical Systems and Signal Processing 132 (2019) 380–404.

[33] G. A. Prieto, J. F. Lawrence, A. I. Chung, M. D. Kohler, Impulse response of civil structures from ambient noise analysis, Bulletin of the Seismological Society of America 100 (2010) 2322–2328.

[34] N. Nakata, R. Snieder, Monitoring a building using deconvolution interferometry. II: Ambient-vibration analysis, Bulletin of the Seismological Society of America 104 (2013) 204–213.

[35] D. Bindi, B. Petrovic, S. Karapetrou, M. Manakou, T. Boxberger, D. Raptakis, K. D. Pitilakis, S. Parolai, Seismic response of an 8-story RC-building from ambient vibration analysis, Bulletin of Earthquake Engineering 13 (2015) 2095–2120.

[36] G. Lacanna, M. Ripepe, M. Coli, R. Genco, E. Marchetti, Full structural dynamic response from ambient vibration of Giotto's bell tower in Firenze (Italy), using modal analysis and seismic interferometry, NDT & E International 102 (2019) 9–15.

[37] E. García-Macías, A. Kita, F. Ubertini, Synergistic application of operational modal analysis and ambient noise deconvolution interferometry for structural and damage identification in historic masonry structures: three case studies of Italian architectural heritage, Structural Health Monitoring (2019).

[38] F. Magalhães, Á. Cunha, Explaining operational modal analysis with data from an arch bridge, Mechanical Systems and Signal Processing 25 (2011) 1431–1450.

[39] F. Ubertini, C. Gentile, A. L. Materazzi, Automated modal identification in operational conditions and its application to bridges, Engineering Structures 46 (2013) 264–278.

[40] M. El-Kafafy, C. Devriendt, G. De Sitter, T. De Troyer, P. Guillaume, Damping estimation of offshore wind turbines using state-of-the art operational modal analysis techniques, in: International conference on Noise and Vibration Engineering, Leuven, Belgium.

[41] M. El-Kafafy, P. Guillaume, B. Peeters, F. Marra, G. Coppotelli, Advanced frequency-domain modal analysis for dealing with measurement noise and parameter uncertainty, in: Topics in Modal Analysis I, Volume 5, Springer, 2012, pp. 179–199.

[42] F. Ubertini, G. Comanducci, N. Cavalagli, A. L. Pisello, A. L. Materazzi, F. Cotana, Environmental effects on natural frequencies of the San Pietro bell tower in Perugia, Italy, and their removal for structural performance assessment, Mechanical Systems and Signal Processing 82 (2017) 307–322.

[43] R. Snieder, M. Miyazawa, E. Slob, I. Vasconcelos, K. Wapenaar, A comparison of strategies for seismic interferometry, Surveys in Geophysics 30 (2009) 503–523.

[44] M. Hubert, M. Debruyne, P. J. Rousseeuw, Minimum covariance determinant and extensions, Wiley Interdisciplinary Reviews: Computational Statistics 10 (2018) e1421.

[45] C. B. Park, R. D. Miller, J. Xia, Imaging dispersion curves of surface waves on multi-channel record, in: SEG Technical Program Expanded Abstracts 1998, Society of Exploration Geophysicists, 1998, pp. 1377–1380.

[46] C. Cornou, M. Ohrnberger, D. M. Boore, K. Kudo, P. Y. Bard, E. Chaljub, F. Cotton, P. Gueguen, Derivation of structural models from ambient vibration array recordings: results from an international blind test, ESG (2006).

[47] G. R. Cowper, The shear coefficient in Timoshenko's beam theory, Journal of Applied Mechanics 33 (1966) 335–340.